



Collaborative enhancement of photon harvesting and charge carrier dynamics in carbon nitride photoelectrode

Miaoyan Huang^{a,b,1}, Yan-Ling Zhao^{a,b,1}, Wei Xiong^{a,b}, Stephen V. Kershaw^c, Yaoguang Yu^{a,d}, Wan Li^c, Tatiana Dudka^c, Rui-Qin Zhang^{a,b,*}

^a Department of Physics and Center for Functional Photonics (CFP), City University of Hong Kong, Hong Kong SAR, China

^b Shenzhen Research Institute, City University of Hong Kong, Shenzhen, China

^c Department of Material Science and Engineering, City University of Hong Kong, Hong Kong SAR, China

^d Department of Chemistry, Harbin Institute of Technology, Harbin, China

ARTICLE INFO

Keywords:

Photoelectrochemical
Graphitic carbon nitride
Boron doping
Water splitting

ABSTRACT

Target-oriented photoelectrochemical (PEC) performance can be enabled by regulating the physicochemical properties of graphitic carbon nitride (CN)-based photoanodes in the PEC process. Herein, we introduced boron heteroatoms into CN films (BCN) and explored the influence of the B heteroatom on the PEC performance experimentally and theoretically. B atoms favor substitution of carbon atoms at bay sites in BCN films and reduce the bandgap by raising the valence band edge as well as constructing optimal electronic structures for PEC hydrogen production. The as-prepared BCN films exhibit nearly 4 times higher photocurrent density than that of pristine CN films. We demonstrate that such enhancement originates from the spatially complementary orbital distribution over the BCN films, thus expediting the charge carrier separation. This work proposes ideal empirical routines for multiple functionalization of CN films for diverse PEC activities via component tailored strategies.

1. Introduction

Artificial photoelectrochemical (PEC) cells that employ semiconductor-based nanomaterials as photoelectrodes are a modern day alternative to natural photosystems for the production of solar fuels. Hydrogen, an energetic molecule that is capable of storing solar energy in the simplest of chemical bonds, can be directly photosynthesized via a PEC water splitting process. Integrating electrochemical systems with light-harvesting absorbers, PEC cells separate the two half reactions for water splitting and show unique advances with respect to powder-based photocatalysis [1]. Lately, graphitic carbon nitride (CN), a stacked two-dimensional (2D) conjugated polymer, has aroused general interest in the field of solar conversion and sustainable development due to its appealing photocatalytic properties [2–8]. Characteristically, CN possesses moderate bandgap energy (~ 2.7 eV), appreciably high chemical stability and is relatively environmentally friendly. Nevertheless, its PEC exploitation is still at a primary phase owing to limited quantum efficiency thus far.

The limitation stems from insufficient long wavelength photon absorption and deficient charge carrier dynamics including a high charge

recombination rate, inadequate carrier lifetime and a confined charge carrier diffusion length [9].

Prior works achieved some amelioration of these shortcomings by engineering CN-based heterojunctions to form 0D [10], 1D [11] and 2D [12] interfaces that facilitate charge transfer processes. Additionally, through atomic level heteroatom doping [13–15] and molecular level copolymerization, tailored functionalization of intrinsic CN materials were successfully demonstrated [16,17]. The approach of doping with foreign elements was very successful in altering CN powders' physical and chemical properties as well as their photocatalytic behaviors. Even so, correlation of the specific enhancement arising from the dopants with the consequential changes in charge carrier dynamics throughout the photocatalysis process remain blurred, let alone the PEC process as a whole.

Aiming at seeking in-depth understanding of the heteroatoms effect on charge transfer processes throughout CN films, herein we tested and simulated the PEC performance of volume boron doped CN films (BCN) experimentally and theoretically [18,19]. We demonstrate that B dopants are energetically favored to substitute at bay site carbon atoms and interrelate closely with the reduction of the bandgap by raising the

* Corresponding author at: Department of Physics and Center for Functional Photonics (CFP), City University of Hong Kong, Hong Kong SAR, China.

E-mail address: aprqz@cityu.edu.hk (R.-Q. Zhang).

¹ These authors contributed equally to this work.

valence band edge. Furthermore, B heteroatoms govern the molecular orbital distribution of modified films, pinning the HOMO distribution mainly on the heptazines incorporated with the B heteroatoms, while the converse is true for the LUMO distribution. The spatially split orbitals consequently enhance the separation between photoholes and photoelectrons thus prolonging carrier lifetime and extending the carrier diffusion length. To the best of our knowledge, thus far, comprehensive perspectives on exploring the effect that heteroatoms exert on the electronic structure and charge carrier dynamics of carbon nitride during the PEC process are still lacking [20–27]. We believe that the present work will shed light on the applicable design guidelines for functionalizing CN films for efficient PEC processes.

2. Experiment section

2.1. Deposition of the CN film

A previously reported thermal vapor condensation (TVC) process was employed to prepare the CN films [17,28,29]. Melamine and boric acid were mixed to prepare precursors. 10 g melamine was dispersed into 30 ml ethanol with stirring at 60 °C for 30 min. Then, 0.4, 0.6, 0.8 and 1 g of boric acid was applied to the dispersions respectively with continuous stirring at 60 °C for another 30 min. Afterwards, the mixtures were kept in a drying oven at 80 °C for 6 h in order to fully exclude the ethanol dispersant. The as-obtained white powders were marked as BCN-0.4, BCN-0.6, BCN-0.8 and BCN-1 depending on the boric acid amount applied, respectively. In a typical TVC routine, a piece of FTO glass (50 mm × 50 mm × 3.2 mm, Sigma-Aldrich, 8Ω/sq) was evenly placed on the top of a fine polished crucible (25 mL) with melamine/boric acid mixtures inside. After that they were transferred into a muffle furnace (Carbolite) and heated to 600 °C with a heating rate of 3 °C/min and kept at 600 °C for 3 h. Before use, the FTO glasses were pretreated in an ultrasound sonication bath in a solution that consisted of acetone (Acros), isopropanol (Acros) and deionized water (18.2 MΩ/cm [2]) with a volume ratio of 1:1:1 for 30 min. After condensation, the FTO glasses coated with CN films were cut into rectangular pieces with identical areas for further evaluation. Each sample was retested for three times using the pieces that cut from different parts of the as prepared thin film (top, middle and bottom).

2.2. Material characterization

X-ray diffraction (XRD) patterns were recorded on a Smartlab X-ray diffractometer (Cu Kα, λ = 1.5406 Å). X-ray photoelectron spectroscopy (XPS) data was obtained from a PHI Model 5802 spectrometer with Al Kα radiation and the peak positions were calibrated by the C 1 s peak at 284.6 eV. The XPS depth profiles were logged with an Argon sputtering rate of 8.22 nm/min. Fourier transform infrared spectroscopy (FTIR) spectra were measured by a Perkin Elmer Spectrum 100 spectrometer. UV/vis spectra were recorded on a Varian Cary 50 spectrophotometer. Steady-state Photoluminescence (PL) spectra of the samples were monitored at room temperature on a Varian fluorescence spectrometer. Time-resolved PL decay curves were recorded on a FLS920 P fluorescence spectrometer (Edinburgh Instruments), equipped with a picosecond pulsed diode laser (EPD-405 nm, pulse width: 48.9 ps) for the PL lifetime (time-correlated single-photon counting; TCSPC) determinations. The photoluminescence decay curves were fitted to a triple-exponential function:

$$I(t) = B_1 e^{-t/\tau_1} + B_2 e^{-t/\tau_2} + B_3 e^{-t/\tau_3}, \quad B_1 + B_2 + B_3 = 1$$

where τ_1 , τ_2 and τ_3 are the decay time constants, and B_1 , B_2 , and B_3 are the normalized amplitudes of each decay component. $\tau_{average}$ is the average lifetime of the decay after the picosecond laser pulse and was calculated according to:

$$\tau_{average} = \frac{B_1 \tau_1^2 + B_2 \tau_2^2 + B_3 \tau_3^2}{B_1 \tau_1 + B_2 \tau_2 + B_3 \tau_3}$$

Plane and cross-sectional views of film morphologies were observed by a JEOL JSM-670 F field-emission scanning electron microscope (FE-SEM). Surface topographies were obtained by (VEECO Multimode V) atomic force microscope (AFM). Raman spectra were acquired from a Horiba Jobin Yvon LabRam HR VIS high-resolution confocal Raman microscope.

2.3. Theoretical calculations

Calculations were carried out using the atomic orbital-based density functional theory (DFT) method implemented in SIESTA code [30]. The DRSLL exchange-correlation functional that involves Van der Waals (VdW) interactions [31,32] and the double zeta plus polarization orbitals basis set were adopted. The detailed parameters used in the calculations include an energy cutoff of 300 Ry, a maximal force threshold of 0.02 eV/Å, a projected atomic orbital energy shift of 10 meV, a maximal displacement tolerance of 1.0×10^{-4} Å, and a k point sampling of $1 \times 1 \times 1$. Note that SIESTA has been successfully applied in many simulations of two-dimensional surfaces [33–35]. The calculations about natural charge population and Wiberg bond order were performed at the level of ωB97XD/6-31G*, which was covered in the Gaussian 09 package [36].

2.4. Photoelectrochemical measurement

The PEC performance of the films was characterized on a three-electrode electrochemical workstation (CHI 760E, Shanghai Chenhua Limited, China) with CN films as the working electrode, platinum foil as the counter electrode and an Ag/AgCl (saturated KCl) reference electrode. Before PEC measurement, the CN films were sealed with epoxy and the effective contact area between CN and electrolyte was kept constantly to be 0.5 cm [2]. The electrolyte consists of 0.2 M sodium sulfate (Na₂SO₄, 99%, Sigma-Aldrich) buffer with (pH = 11.7) and without (pH = 7) 0.05 M sodium sulfide (Na₂S, 99%, Sigma-Aldrich). The potentials referred to Ag/AgCl were converted into reversible hydrogen electrode (RHE) potentials according to the Nernst equation:

$$E_{RHE} = E_{Ag/AgCl} + 0.059 \text{ V} \times \text{pH} + E^{\circ}_{Ag/AgCl}$$

where $E^{\circ}_{Ag/AgCl} = 0.197 \text{ V}$ at 25 °C.

PEC measurements were carried out under illumination of an air mass 1.5 global (AM 1.5 G) solar simulator (NewBet HSX-F300) with a calibrated power density of 100 mW/cm [2]. The possible light incident directions consisted of two types: from electrode to electrolyte (EE illumination) and from substrate to electrode (SE illumination). Unless specified otherwise, EE illumination was employed during PEC measurements. The Nyquist plots were made at open circuit voltage conditions with a frequency range from 0.1 Hz to 100 kHz and AC voltage of 10 mV. The incident light-to-electron current conversion efficiency (IPCE) of the films was calculated according to the following equation:

$$\text{IPCE}(\lambda) = \frac{1240(\text{V} \times \text{nm}) \times J_{ph}(\text{mA}/\text{cm}^2)}{\lambda(\text{nm}) \times P_{mono}(\text{mW})}$$

where λ and P_{mono} are the wavelength and the power of the incident monochromatic light generated by the monochromator (SOFN 71MU1021), and J_{ph} is the photocurrent density. Mott-Schottky plots involved measuring the space charge layer capacitances (C_{sc}) of CN films upon applied bias according to:

$$\frac{1}{C_{sc}^2} = \frac{2}{\epsilon_r \epsilon_0 A^2 e N_d} \left(E - E_{fb} - \frac{kT}{e} \right)$$

where

ϵ_r , ϵ_0 , e and A stand for the relative permittivity of the semiconductor, the vacuum permittivity, the charge of an electron and the

effective surface area of the semiconductor, respectively; N_d is the free carrier density; E represents the applied potential and E_{fb} is the flat band potential; k denotes the Boltzmann constant, T is the absolute temperature. Mott-Schottky plots were acquired in the dark with a sinusoidal modulation at a frequency of 3000 Hz.

3. Results and discussion

Initially, we applied boric acid and melamine as the boron heteroatom source and polymerization precursor, respectively. For fundamental evaluation of PEC activities, different amount of boric acid were added into melamine (see the Experimental section) and denoted as BCN-0.4, BCN-0.6 and BCN-0.8 (BCN- x), respectively. After condensation, the as-prepared pristine CN films (see Supporting information Figure S1) and the BCN- x films bear distinct morphologies, with the nanoparticle size becoming larger according to the B doping level (see Figure S2). AFM three-dimensional topographies (see Figure S7) unveil that B dopants introduced a more rough film surface texture. BCN- x films show distinct film morphology compared with the pristine CN films and correlates with their different physicochemical properties.

The surface composition of pristine CN and BCN- x films were then characterized by XPS analysis. The spectra of C 1s (cf. Fig. 1a) can be deconvoluted into two distinct binding species, specifically, the C–N = C bond locates at 288.2 eV and absorbed sp^2 C contamination locates at 284.6 eV [37,38]. The intensity of the former peaks decrease compared to that of the latter with increasing boron content, suggesting a shrinking amount of C–N = C bonds in BCN- x films. As presented in Fig. 1b, three deconvoluted N 1s peaks of pristine CN films depict the C–N = C (398.5 eV), N–C3 (399.9 eV) and C–N–H (400.8 eV) bonds, respectively. [39,40] A new N 1s peak with binding energy of 399.2 eV emerges for BCN- x films, and can be assign to C–N–B bonds [41]. The single B 1s peaks center at 191 eV for BCN- x films is consistent with the binding energy of the C–NB group for BCN compound (Fig. 1c) [42–44]. No peak around 190 eV is observed, suggesting that BCN- x films are free from B–N as that existing in h-BN. Absence of B–C bonds with binding energy of 189.4 eV, signified that carbon atoms were substituted by boron heteroatom in the BCN- x matrix [45]. Noting that XPS characterization is incapable of disclosing the specific substitution sites in CN monoliths, we carried out DFT computations. The total energy of BCN- x with B embedded in the bay carbon sites is 0.26 eV lower than that of corner carbon sites, indicating bay sites are more energetically favorable for B atoms substitution (cf. Fig. 1e), in accordance with previous reports [18,46]. Therefore, all the following calculations were based on the situation that boron atoms substituted bay sites carbon atoms.

To identify whether B dopants bring any structural change into modified films, the crystalline phase of pristine CN and BCN- x films were studied by XRD (Fig. 1d). The characteristic peaks at 27.5° in the diffraction pattern that arises from interlayer stacking is broadened and attenuated with enhanced boron dopant content in the matrix. The structural variation for BCN- x films originates from the dissimilar atomic radii between boron (8.7 Å) and carbon (6.7 Å) atoms. With B atom incorporation into the CN matrix, the layer stacking is destroyed. The chemical structure was further verified by Fourier transform infrared and Raman spectroscopy (cf. Figure S2). The lack of new bands arising suggests that B dopants preserve the local CN structure and this is consistent with the XRD results.

With successful incorporation of B heteroatoms into the CN matrix at bay sites, we evaluated pristine CN and BCN- x films as photoanodes to investigate the B dopant's impact on PEC activities. PEC performance was conducted in a three-electrode configuration with electrolyte (pH = 11.7) consisting of 0.2 M Na_2SO_4 and 0.05 M Na_2S . Linear sweep voltammetry (LSV) measurement was carried out under chopped simulated AM 1.5 G illumination (time interval: 20 s). As shown in Fig. 2a, BCN-0.6 film boosts the photocurrent density to 55 $\mu A/cm^2$ [2] while BCN-0.8 corrupts the photocurrent density to 10 $\mu A/cm^2$ [2] at

1.23 V vs. RHE. With moderate amount of B dopants embedded, the photocurrent of BCN-0.6 film is intensified by a factor of $\times 3.6$ with respect to that of pristine CN film (PEC performance of reported bare CN photoanodes is summarized in Table S2). The enhanced PEC performance implies an assisted charge migration and collection process in BCN-

0.6 films. Electrochemical impedance spectroscopy (EIS) measurement further evidences the facilitated charge migration process in modified films. The Randles-Ershler (R-E) circuit model was adopted as the equivalent circuit to simulate the PEC process as shown in Fig. 2b inset. The resistor R_s represents the contact resistance between the electrolyte and the external electrical circuit. R_{ct} is the resistor related to the charge transfer process at the interface between the photoanode and electrolyte. The arc diameters of the semicircles achieved in Nyquist plots show the magnitude of corresponding R_{ct} at the electrolyte and electrode interface (Supporting Information Figure S12). The smaller size of the semicircle arc diameter indicates a more effective separation of charge carriers or a faster charge transfer process at the interface. A decreased semicircle is observed for BCN- x films with increasing B dopants content as present in the Nyquist plot (cf. Fig. 2b and Supporting Information Figure S13), demonstrating introduced B atoms suppress the charge transfer resistance between the electrode and electrolyte interface [47]. To determine the electron collection efficiency per incident photon flux at each wavelength, incident light-to-electron current conversion efficiency (IPCE) was obtained at 1.23 V vs. RHE (cf. Fig. 2c). The IPCE plots reveal a superior conversion efficiency of moderate amount of B doped films compared to that of pristine CN films, for BCN-0.6 it is nearly 4% at 400 nm and is 8 times higher than that of pristine CN. Thence, under visible light illumination ($\lambda > 420$ nm), BCN-0.6 film can give rise to a photocurrent that is twice as much as that of pristine CN film (Fig. 2c: inset). While, for BCN-0.8 film, the IPCE drops to 1%, since dopants introduce excessive defect levels in the bulk of the semiconductor that degrade the charge collection efficiency. Apart from the excessive defect levels that B atoms bring in, BCN-0.8 films also bear larger nanoparticles that contain more grain boundaries inside. The grain boundaries feature energy barriers and hinder the charge migration.

To address the origin for the distinct PEC performance of BCN- x films, we further characterized the physicochemical properties of the modified films. With regards to fulfilling the utilization of solar energy, the optical characteristic was first probed by UV–vis diffuse reflectance spectra (Fig. 2d) and the optical bandgap was evaluated from a Tauc plot (Fig. 2d: inset) [48]. Accordingly, the photon harvesting capability of BCN films is enhanced compared to that of the pristine CN film accompanied with a noticeable red shifted absorption onset when all the films possess nearly identical thickness (62.1 ± 4.3 nm). Optical bandgap energies fall from 2.77 to 2.60 eV with increasing B dopant content, extending the photon absorption edge into the visible light region. Even through it is of great importance to make full use of visible-light, which accounts for 53% in the solar spectrum, a diminished bandgap energy would on the other hand be detrimental to the carrier kinetics driving efficient water redox reactions by electron-hole pairs in PEC cells.

To further define how B dopants modify the electronic structure and affect the thermodynamic driving force for water redox reactions in BCN films, valence band (VB) structure investigation was performed by XPS. VB maxima are interpreted to be at 1.86, 1.74, 1.63 and 1.35 eV for pristine CN, BCN-0.4, BCN-0.6 and BCN-0.8 correspondingly by fitting the linear part of the spectra (Supporting information Figure S4a). Combined with the optical bandgap energies obtained previously, the conduction band (CB) minimum of BCN- x films are derived to be slightly raised compared to that of pristine CN. In order to estimate whether the band alignment straddle the water redox potentials, the band structures for pristine CN and BCN- x films were delineated (Figure S4b). Interestingly, it turns out that the bandgap reduction mechanism for BCN- x films is the B dopants raising the valence band edge rather

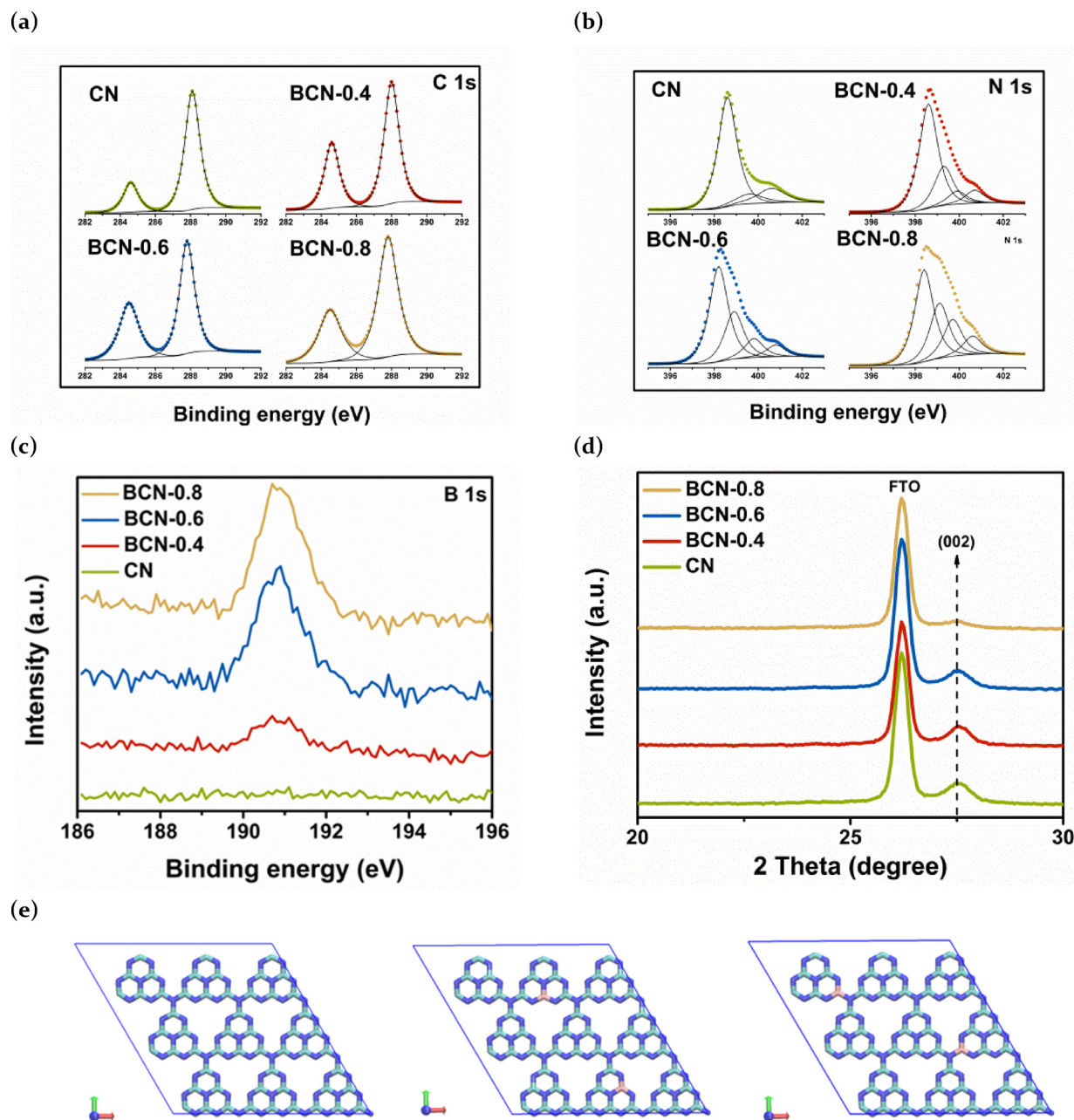


Fig. 1. The XPS spectra of (a) C 1 s, (b) N 1 s and (c) B 1 s; (d) XRD patterns; (e) Top views of supercell 3 × 3 pristine CN (left) and BCN-0.6 with two C substituted by B at corner (middle) and bay (right) sites in a lattice with constants of $a = b = 21.04 \text{ \AA}$, $c = 20.0 \text{ \AA}$, and $\alpha = \beta = 90^\circ$, $\gamma = 120^\circ$ by DFT optimizations (VDW/DRSLL). The doping atomic ratio between C and B is 26:1 (corresponding to the composition of BCN-0.6 that determined by XPS). The green, blue, and pink colors represent C, N, and B atoms, respectively. (For interpretation of the references to colour in this figure legend, the reader is referred to the web version of this article).

than lowering the conduction band edge. Photoelectrochemically, the slightly raised conduction band edge of the photoelectrodes would improve the overpotential to $E(\text{H}^+/\text{H}_2)$ thus boosting hydrogen yields. Therefore, B heteroatoms would reduce the bandgap of CN efficiently without sacrificing hydrogen production.

To fully understand how the B dopant modifies BCN- x electronic structures, it is important to determine the band structure as well as the band alignment through PEC measurement based on the Mott-Schottky (MS) relationship. By interpreting MS plots, the influence that B heteroatoms exert on the flat band potential and free carrier density can be determined [49]. As shown in Fig. 3a, all the curves possess positive slopes defining their n-type characteristic. The steepest slope of pristine CN film indicated the lowest free carrier density. Where more B heteroatoms were introduced the free carrier density increased

accordingly. Generally, the improved charge carrier density guarantees improved bulk electrical conductivity. In addition, the intercept also shifted as more B atoms doping level was increased, signifying a significant band bending in the space charge region. The intensified band bending enhances the separation of charge carriers, slows the charge recombination rate at the electrode and electrolyte interface and is in agreement with the Nyquist plot. The determination of the conduction band minimum of all the films by the MS method is in approximate agreement to the values estimated by XPS data, with the CB edge raised slightly under B doping conditions.

Motivated by the above appealing findings, we sought more support for our model from DFT studies by investigating the impact of B atoms on the electronic structure of the BCN-0.6 film. After the incorporation of B dopants, the bandgap energy of CN films is found to be narrowed

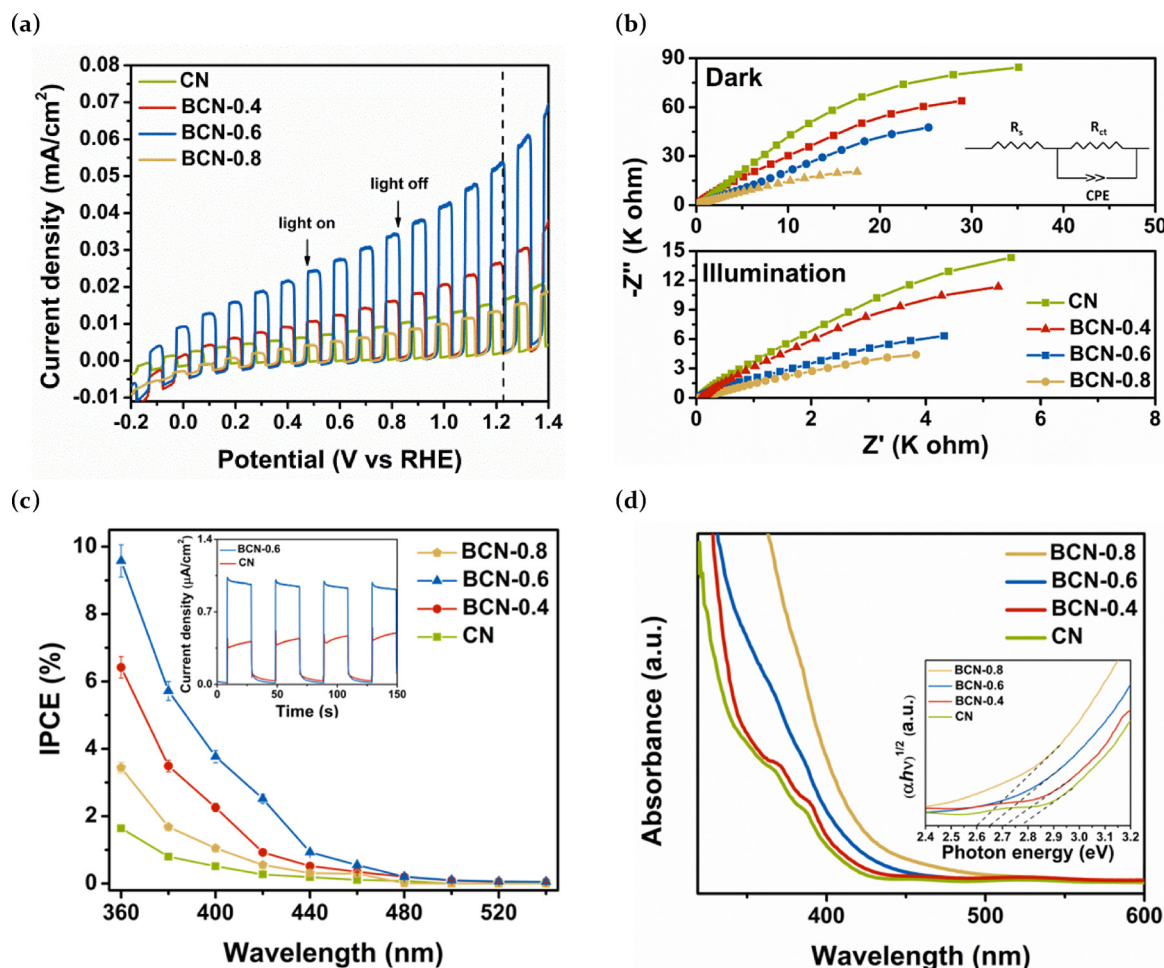


Fig. 2. (a) The light chopped LSV curves; electrolyte: 0.2 M Na₂SO₄ and 0.05 M Na₂S (pH = 11.7), (b) the Nyquist plots under illumination and in the dark condition (inset: the equivalent circuit adopting the Randles–Ershler circuit model), (c) the IPCE spectra with transient photocurrent density curves under visible light ($\lambda > 420$ nm) inset, and (d) the UV–vis absorption spectra and Tauc plot (inset).

from 0.66 to 0.54 eV (see Fig. 3b). Although the bandgap of pristine CN here is underestimated with respect to the experimental value (2.77 eV) due to the well-known limitation of DFT [50], the relative value of ~ 0.12 eV effectively reflects the significant alternation of the electronic property of BCN-0.6 films, in agreement with our experimental results. The valence band of BCN-*x* is dramatically upshifted, and this is attributed to the replacement of B heteroatoms into the CN backbone with new B–N bonds formed. To gain a further insight into the intrinsic reason for causing the electronic structure change, we carried out natural bond order (NBO) calculations at the level of ω B97XD/6-31G* based on the hepazine cluster with two C atoms at the bay sites replaced by B heteroatoms. As labeled in Figure S5, the Wiberg bond order between B and three N atoms (1.0, 1.0, 0.8) is generally lower than that of C and three N atoms (1.4, 1.4, 1.0), indicating that weaker B–N bonds would induce their electrons to be located at higher energy levels. As shown in Fig. 3b, the PDOS of two B atoms indeed has a non-negligible distribution near the valence band top. B incorporation into CN film generates a remarkable impact on frontier molecular orbital alignment so as to rearrange the electronic structure of the resulting BCN-*x* films. The natural partial atomic (NPA) charge was also calculated for BCN-0.6 film (see Figure S6). The positive NPA charge on two B (+1.007, +1.008) implies that the B atom plays a role of a ready donor in BCN-*x* film with electron transferred from B to adjacent N atoms. The NPA charge on C is generally about +0.6 to +0.7. Combining the BO results with the NPA charge picture, we understand that the bond strength and bond property are markedly different between B–N and C–N.

With the above understanding of the modified electronic structures

in BCN-*x* films, we next sought to rationalize the advancement in charge migration dynamics that result from the evolved band structure of BCN-*x* films. PL spectra were measured to highlight changes in the charge recombination rates in the films. Quenching of the PL intensity for significantly B doped CN films denotes a lower charge recombination rate with respect to pristine CN films (Fig. 3c). Likewise, as observed in the fitted PL decay lifetime curves (Fig. 3d, Table S1), BCN-0.6 possesses the longest carrier lifetime, suggesting that B dopants primarily extend the charge carrier lifetime. However, beyond an optimum level further increases in B doping levels in the CN matrix then reversed this trend and shortened the carrier lifetime by shrinking the ordered domains and attenuating semiconductor characteristics as previously discussed. Additionally, the fact that BCN-*x* films showed a slightly delayed PL decay compared to pristine CN indicates that BCN-*x* films hold more surface defects giving rise to shallow traps. To exclude the contributions from surface doping and nanojunction formation, which separate the electron and hole by internal energy level difference rather than the atomic dopant effects we wished to probe, we measured the XPS depth profile of our samples (Figure S7) [18,19]. B dopants are found to distribute homogeneously within the CN films, which leads to the efficient charge separation results seen from the modification with B dopants rather than the creation of nanojunction interfaces. Charge carrier diffusion length is another crucial factor during charge transfer process in PEC cells, therefore, the photoresponse of pristine CN and BCN-0.6 films was studied under EE and SE illumination individually. Pristine CN yields superior photocurrent under EE illumination compared to that under SE illumination (Figure S8), implying that it suffers

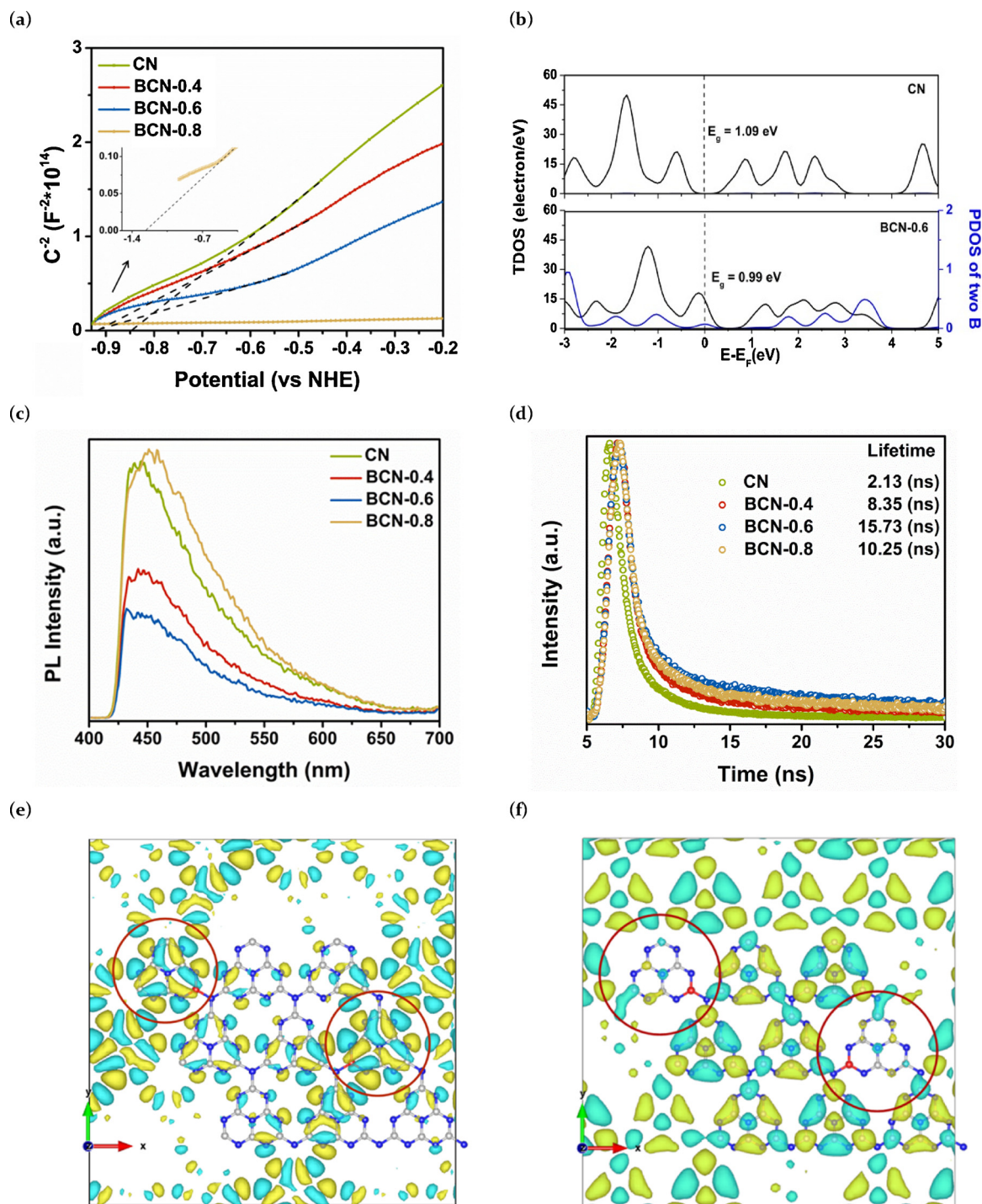


Fig. 3. (a) Mott-Schottky plots. (b) Density of states (DOS) of pristine CN and BCN-0.6 with two bay sites carbon atoms substituted by B atoms by DFT calculations. Projected DOS of two B atoms is presented in blue curve. (c) PL spectra (with a 430 nm short wavelength cut-off filter). (d) PL decay curves for 470 nm emission peak. (e) Molecular orbitals (MOs) of the valence band top and (f) conduction band bottom on a 3×3 unit cell of one-layer BCN-0.6 from DFT calculations (VDW/DRSLL) with the energy cutoff 300 Ry. The Fermi level is -4.658 eV for BCN-0.6; the MO energy eigenvalues are shown in parentheses. Lattice parameters are $a = b = 21.04$ Å, $c = 20.0$ Å, and $\alpha = \beta = 90^\circ$, $\gamma = 120^\circ$. Each orbital is shown in top view and C, N, and B atoms are colored in grey, blue and red. Yellow and blue regions represent the MO wave function with two opposite phases. The isovalue is set as 0.009 a.u. to give a clearer illustration. (For interpretation of the references to colour in this figure legend, the reader is referred to the web version of this article).

from insufficient hole diffusion length (less than the film thickness). BCN-0.6 film, by contrast, generates nearly identical photocurrent under EE and SE illumination, pointing to a longer carrier diffusion length that is nearly equivalent to the film thickness (~ 60 nm). Additionally, without the utilization of the hole scavenger Na_2S , pristine CN films show a sharp drop in photocurrent density owing to

insufficient minority carrier mobility. In contrast, BCN-0.6 films exhibit negligible decrease of photocurrent density with the hole scavenger absent, indicating enhanced charge carrier dynamics with B atoms introduced. Comparing the photocurrent density of pristine CN and BCN-0.6 films under two types of illumination, we can conclude that B atom incorporation primarily improves the minority carrier (hole)

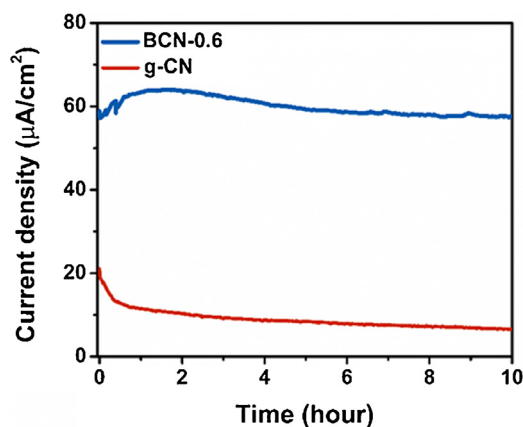


Fig. 4. Transient photocurrent density of pristine CN and BCN-0.6 films over 10 h at 1.23 V versus RHE under EE illumination.

transportation.

To get a comprehensive insight into the role that B dopants play in the charge transfer process throughout BCN-*x* films at the atomic level, the highest occupied molecular orbitals (HOMO) and the lowest unoccupied molecular orbitals (LUMO) was imaged by DFT calculation. For pristine CN, HOMO and LUMO are homogeneously distributed over the CN monolith (see Figure S9). However, this is not the case for BCN-0.6 as shown in Fig. 3e. After the B dopants were introduced, the HOMO (valence band top) became much more localized onto two hepazines, meanwhile, the LUMO (conduction band bottom) becomes a little bit delocalized. The localized HOMO is due to the single bond of B–N breaking the original π -conjugation between C and N. Interestingly, the distribution of HOMO and LUMO is spatially complementary in B modified CN monolith (i.e., the electrons of HOMO are mainly distributed on the hepazines with B incorporated, while the LUMO has a distribution on the hepazines without B dopants as highlighted in Fig. 3e and f). This suggests that the recombination of electron and hole after illumination can be suppressed due to the B doping. The calculations provide solid evidence to support our experiment results that B dopants promote the charge transport dynamics, especially for holes, during the PEC process by prolonging carrier lifetime and carrier diffusion length effectively.

Photostability was assessed for practical long-term PEC applications. As presented in Fig. 4, BCN-0.6 film shows a considerably high photostability and maintains 90% of initial photocurrent under 10 h illumination. Unlike the BCN-0.6 film, the pristine CN film lost 93% of the initial photocurrent over the 10 h PEC process. The remarkably high photostability of BCN-0.6 films originate from the efficient extraction of photogenerated holes from the near surface region thus reducing chemical attack on the C–N bond. Additionally, nitrogen atoms can be stabilized by boron instead of carbon, for instance, graphitic materials that consist of carbon and nitrogen are not as thermally stable as h-BN [51]. Thus, the superficial B–N bonds in BCN-0.6 films are not easily broken by oxidizing species as the C–N bonds, ensuring greater long-term stability. The films after PEC tests were also investigated by AFM (Figure S10) and SEM (Figure S11), it turns out that the film thickness and roughness increase after the test with aggregations of the nanoparticles. The increase of thickness and roughness for pristine CN films is more severe than that for BCN-0.6 films, indicating that pristine CN films degrade more substantially than BCN-0.6 films and that therefore B dopants improve the photostability rather effectively.

4. Conclusion

In summary, we employed a TVC method to deposit boron doped carbon nitride films as high-performance PEC photoanodes. The modified films exhibited improvements in long wavelength photon

harvesting and charge transfer processes and therefore yielded 3.6 times magnified photocurrent density with considerably better photostability compared to that of pristine CN films. Notably, the experimental and theoretical studies revealed that B dopants could render a reduced bandgap by raising the valence band position and also elongate the charge carrier lifetime by altering orbital distributions. Our results emphasize the significance of component tailored design in CN-based photoanodes which can further advance the use of CN films' photocatalytic properties for a number of PEC applications.

Acknowledgements

This work was supported by grants from the Research Grants Council of the Hong Kong SAR [project no. CityU11334716], Basic Research Programs in Shenzhen, China [project nos. JCYJ20150601102053060 and JCYJ20160215152550988] and the Centre for Functional Photonics of City University of Hong Kong. This work was financially supported by the Guangdong-Hong Kong Technology Cooperation Funding Scheme (2017A050506048).

Appendix A. Supplementary data

Supplementary material related to this article can be found, in the online version, at doi:<https://doi.org/10.1016/j.apcatb.2018.06.046>.

References

- [1] M.G. Walter, E.L. Warren, J.R. McKone, S.W. Boettcher, Q. Mi, E.A. Santori, N.S. Lewis, *Chem. Rev.* 110 (2010) 6446–6473.
- [2] K. Wang, Q. Li, B. Liu, B. Cheng, W. Ho, J. Yu, *Appl. Catal. B Environ.* 176 (2015) 44–52.
- [3] X. Wang, X. Chen, A. Thomas, X. Fu, M. Antonietti, *Adv. Mater.* 21 (2009) 1609–1612.
- [4] X. Wang, K. Maeda, A. Thomas, K. Takanabe, G. Xin, J.M. Carlsson, K. Domen, M. Antonietti, *Nat. Mater.* 8 (2009) 76–80.
- [5] Y. Wang, Y. Di, M. Antonietti, H. Li, X. Chen, X. Wang, *Chem. Mater.* 22 (2010) 5119–5121.
- [6] Y. Zheng, L. Lin, B. Wang, X. Wang, *Angew. Chemie Int. Ed.* 54 (2015) 12868–12884.
- [7] G. Liu, P. Niu, C. Sun, S.C. Smith, Z. Chen, G.Q. Lu, H.-M. Cheng, *J. Am. Chem. Soc.* 132 (2010) 11642–11648.
- [8] H. Huang, S. Yang, R. Vajtai, X. Wang, P.M. Ajayan, *Adv. Mater.* 26 (2014) 5160–5165.
- [9] J. Zhang, M. Zhang, L. Lin, X. Wang, *Angew. Chemie* 127 (2015) 6395–6399.
- [10] Y. Liu, K. Yan, J. Zhang, *ACS Appl. Mater. Interfaces* 8 (2015) 28255–28264.
- [11] C. Chang, L. Zhu, S. Wang, X. Chu, L. Yue, *ACS Appl. Mater. Interfaces* 6 (2014) 5083–5093.
- [12] Z. Zhang, J. Huang, M. Zhang, Q. Yuan, B. Dong, *Appl. Catal. B Environ.* 163 (2015) 298–305.
- [13] G. Zhang, M. Zhang, X. Ye, X. Qiu, S. Lin, X. Wang, *Adv. Mater.* 26 (2014) 805–809.
- [14] Z.F. Huang, J. Song, L. Pan, Z. Wang, X. Zhang, J.J. Zou, W. Mi, X. Zhang, L. Wang, *Nano Energy* 12 (2015) 646–656.
- [15] H. Wang, X. Zhang, J. Xie, J. Zhang, P. Ma, B. Pan, Y. Xie, *Nanoscale* 7 (2015) 5152–5156.
- [16] J. Zhang, G. Zhang, X. Chen, S. Lin, L. Möhlmann, G. Dolega, G. Lipner, M. Antonietti, S. Blechert, X. Wang, *Angew. Chemie* 124 (2012) 3237–3241.
- [17] J. Bian, L. Xi, C. Huang, K.M. Lange, R.Q. Zhang, M. Shalom, *Adv. Energy Mater.* 6 (2016) 1600263.
- [18] Q. Ruan, W. Luo, J. Xie, Y. Wang, X. Liu, Z. Bai, C.J. Camalt, J. Tang, *Angew. Chemie Int. Ed.* 56 (2017) 8221–8225.
- [19] C.S. Guo, L.B. Luo, G.D. Yuan, X.B. Yang, R.Q. Zhang, W.J. Zhang, S.T. Lee, *Angew. Chemie Int. Ed.* 48 (2009) 9896–9900.
- [20] J. Zhu, T. Diau, W. Wang, X. Xu, X. Sun, S.A.C. Carabineiro, Z. Zhao, *Appl. Catal. B Environ.* 219 (2017) 92–100.
- [21] L. Wang, S. Thaweesak, S. Wang, M. Lyu, M. Xiao, P. Peerakiatkhajohn, *Dalt. Trans.* 46 (2017) 10714–10720.
- [22] N. Sagara, S. Kamimura, T. Tsubota, T. Ohno, *Appl. Catal. B Environ.* 192 (2016) 193–198.
- [23] C. Lu, R. Chen, X. Wu, M. Fan, Y. Liu, Z. Le, S. Jiang, S. Song, *Appl. Surf. Sci.* 360 (2016) 1016–1022.
- [24] S. Liu, *Catal. Sci. Technol.* 6 (2016) 7002–7023.
- [25] H. Li, Y. Liu, X. Gao, C. Fu, X. Wang, *ChemSusChem* 8 (2015) 1189–1196.
- [26] Z. Lin, X. Wang, *Angew. Chemie Int. Ed.* 52 (2013) 1735–1738.
- [27] Q. Gu, J. Liu, Z. Gao, C. Xue, *Chem. Asian J.* 710062 (2016) 3169–3173.
- [28] J. Bian, J. Li, S. Kalytchuk, Y. Wang, Q. Li, T.C. Lau, T.A. Niehaus, A.L. Rogach, R.Q. Zhang, *ChemPhysChem* 16 (2015) 954–959.
- [29] J. Bian, Q. Li, C. Huang, J. Li, Y. Guo, M. Zaw, R.Q. Zhang, *Nano Energy* 15 (2015)

- 353–361.
- [30] A. Pecchia, J.M. Soler, E. Artacho, J.D. Gale, A. García, J. Junquera, P. Ordejón, D. Sánchez-Portal, *J. Phys. Condens. Matter* 14 (2002) 2745–2767.
- [31] G. Román-Pérez, J.M. Soler, *Phys. Rev. Lett.* 96102 (2009) 1–4.
- [32] M. Dion, H. Rydberg, E. Schröder, D.C. Langreth, B.I. Lundqvist, *Phys. Rev. Lett.* 1 (2004) 22–25.
- [33] A. Hauschild, K. Karki, B.C.C. Cowie, M. Rohlfing, F.S. Tautz, M. Sokolowski, *Phys. Rev. Lett.* 36106 (2005) 1–4.
- [34] A.S. Foster, M.A. Gosálvez, T. Hynninen, R.M. Nieminen, K. Sato, *Phys. Rev. B* 76 (2007) 1–8.
- [35] R. Coquet, G.J. Hutchings, S.H. Taylor, D.J. Willock, *J. Mater. Chem.* 16 (2006) 1978–1988.
- [36] M.J. Frisch, G.W. Trucks, H.B. Schlegel, G.E. Scuseria, M.A. Robb, J.R. Cheeseman, G. Scalmani, V. Barone, B. Mennucci, G.A. Petersson, Gaussian 09, Revision C. 01, Gaussian, Inc., Wallingford, CT, 2009.
- [37] S. Yan, Z. Li, Z. Zou, *Langmuir* 25 (2009) 10397–10401.
- [38] D.J. Martin, K. Qiu, S.A. Shevlin, A.D. Handoko, X. Chen, Z. Guo, J. Tang, *Angew. Chemie Int. Ed.* 53 (2014) 9240–9245.
- [39] S. Yan, Z. Li, Z. Zou, *Langmuir* 26 (2010) 3894–3901.
- [40] L. Lai, J.R. Potts, D. Zhan, L. Wang, C.K. Poh, C. Tang, H. Gong, Z. Shen, J. Lin, R.S. Ruoff, *Energy Environ. Sci.* 5 (2012) 7936–7942.
- [41] J. Wang, J. Hao, D. Liu, S. Qin, D. Portehault, Y. Li, Y. Chen, W. Lei, *ACS Energy Lett.* 2 (2017) 306–312.
- [42] L. Song, L. Ci, H. Lu, P.B. Sorokin, C. Jin, J. Ni, A.G. Kvashnin, D.G. Kvashnin, J. Lou, B.I. Yakobson, *Nano Lett.* 10 (2010) 3209–3215.
- [43] J.A. Schreifels, P.C. Maybury, W.E. Swartz, *J. Catal.* 65 (1980) 195–206.
- [44] X. NIST, ray Photoelectron Spectroscopy Database, NIST Standard Reference Database 20, Version 4.1, (2012).
- [45] M. Kawaguchi, T. Kawashima, T. Nakajima, *Chem. Mater.* 8 (1996) 1197–1201.
- [46] Y. Wang, H. Li, J. Yao, M. Antonietti, *Chem. Sci.* 2 (2011) 446–450.
- [47] H. Liu, S. Cheng, M. Wu, H. Wu, J. Zhang, W. Li, C. Cao, *J. Phys. Chem. A* 104 (2000) 7016–7020.
- [48] O. Stenzel, *The Physics of Thin Film Optical Spectra*, Springer, Switzerland, 2016.
- [49] M.E. Orazem, B. Tribollet, *Electrochemical Impedance Spec-Troscopy*, John Wiley & Sons, Inc., New York, 2011.
- [50] X.G. Ma, Y.H. Lv, J. Xu, Y.F. Liu, R.Q. Zhang, Y.F. Zhu, *J. Phys. Chem. C* 116 (2012) 23485–23493.
- [51] X.X. Fu, R.Q. Zhang, *Energetics of hexagonal boron nitride nanostructures: edge dependence and truncation effects*, *Nanoscale* 9 (2017) 6734–6740.